Int J Adv Manuf Technol (2013) 65:895–907
DOI 10.1007/s00170-012-4226-9

ORIGINAL ARTICLE

Gyroscopic and mode interaction effects on micro-end mill dynamics and chatter stability

Yinuo Shi · Frederik Mahr · Utz von Wagner · Eckart Uhlmann

Received: 5 December 2011 / Accepted: 7 May 2012 / Published online: 22 May 2012

Abstract This paper investigates the gyroscopic and mode interaction effects on the micro-end mill dynamics and the stability behavior due to regenerative chatter. A high-speed spindle system for micro-milling is modeled using finite elements. The transfer functions and the mode shapes are studied to gain a deep insight into the dynamic characteristics. The experimentally identified chatter states and operational vibration modes are given to verify the analytical results. It is shown that, due to the small rotary inertia of the micro-end mill, the gyroscopic effect considered in the inertial frame is less significant despite high rotational speeds. The mode interaction strongly affects the dynamics and the chatter stability. Moreover, piezoelectric elements are applied to in-process excitation in order to identify the transfer behavior of the micro-end mill in the operating state.

Keywords Micro-end mill dynamics · Gyroscopic effect · Transfer function · Mode shape · Mode interaction · In-process excitation

Y. Shi · U. von Wagner (✉)
Department of Applied Mechanics, Chair of Mechatronics and Machine Dynamics, Technische Universität Berlin, Einsteinufer 5-7, 10587 Berlin, Germany
e-mail: utz.vonwagner@tu-berlin.de

Y. Shi
e-mail: yinuo.shi@tu-berlin.de

F. Mahr · E. Uhlmann
Institute for Machine Tools and Factory Management, Technische Universität Berlin, Pascalstraße 8-9, 10587 Berlin, Germany

1 Introduction

Regenerative chatter is known as an unstable phenomenon arising in machining processes and leading to poor product quality, tool wear, and even tool damage. However, chatter analysis in micro-cutting operations has not been extensively investigated compared to that of macro machining [1–3]. More structural and process influences should be taken into account, e.g., the feed rate effect due to the existence of different cutting zones [4–6].

Micro-cutting operations are conducted at high rotational speeds. The spindle dynamics should be studied considering diverse aspects [7, 8], such as the changes of bearing stiffness, the gyroscopic effect, and the misalignment. For chatter analysis, however, the tool dynamics must also be involved. The stability behavior is strongly influenced by the dynamics of the tool end point. Movahhedy and Mosaddegh [9] studied the gyroscopic effect on the chatter stability in high-speed milling based on the finite element (FE) model of the spindle. Their numerical results showed that the backward mode prominently decided the chatter stability. In micro-milling operations, the spindle speeds are much higher, but the mass and the radius of the micro-end mill are much smaller. How is that case in micro-milling?

Besides, as Riven pointed out in [10], the tooling structure significantly affected the machine tool dynamics. In order to predict the dynamics of the tool tip point, the stiffness and damping properties of the clamping positions should also be taken into account. The imperfect clamping conditions at the spindle–tool holder–tool (STT) interfaces could result in erroneous estimation of the natural frequencies while

modeling tools as cantilever beams with the free overhang length (projected from the first built-in point to the tool tip point) only [10–12]. The tool tip dynamics is affected by different machine tool components due to their mode interactions. Marui et al. [13] investigated the contact rigidity between tool shank and tool holder in turning. The spring constants were estimated for different clamping forces and different tools by simple empirical expressions. Smith et al. [14] experimentally studied the drawbar force effect on the spindle–tool holder joint. The changes of the resonance frequencies as well as the magnitudes of the peaks at different drawbar forces indicated the changes of the stiffness and damping properties at the spindle–tool holder interface. Luo et al. [15] studied the effects of the tooling structural characteristics on the surface generation and verified their significance for the machined surface quality. Albertelli et al. [16] presented the effects of the interactions between spindle–control–machine subsystems on the tool tip dynamics and thus on the cutting process stability. Using the substructure coupling technique [17–19], the interactions of the component modes were presented in [20], where the so-called dynamic absorber effect in high-speed machining was particularly studied for diverse tool overhang lengths. Another type of mode interaction in milling is deduced by the cutting forces in different mode directions. Zatarain et al. [21] studied this mode coupling effect due to the directional force factors.

The joint parameters of a machine tool model, on the other hand, are usually estimated from the measured tool tip transfer functions. However, it is challenging to directly measure the transfer functions in micro-milling. Due to the small size of the micro-end mills, noncontact excitation and response measurements are required to avoid the alteration of the tool tip dynamics. In addition, excitation with a sufficient frequency bandwidth should be employed since the dominant natural frequencies of the machine tool system are usually much higher than those in conventional milling. Using substructure coupling analysis, the tool tip transfer functions and the joint parameters can be semi-analytically determined [17–19]. Mascardelli et al. [11] applied this method to micro-end mills by extending the experimental data from 10 to 150 kHz. Filiz and Ozdoganlar [22, 23] employed piezoceramic materials to excite the micro-scale tools under free–free boundary conditions. They identified the transfer functions up to 100 kHz, but the tools were not coupled to the spindle system. In the field of break squeal, using piezoelectric elements, the transfer functions of the rotating disk brakes have been measured by von Wagner et al. [24–27]. This method can be employed in micro-machining to realize the in-process excitation. Together with the response signals measured, e.g., by a laser vibrometer, the transfer behavior in the operating state can be identified.

This paper is organized as follows. Section 2 presents the FE model of the spindle system and the micro-end mill by treating the element as Timoshenko beam. The equations of motion are derived with respect to the inertial and rotating frames and compared with each other. In Section 3, piezoelectric elements are adopted to identify the transfer behavior of the micro-end mill during cutting processes. In Section 4, the gyroscopic effect on the micro-end mill dynamics and chatter stability is studied by both analytical and experimental results. The effects of mode interaction and joint flexibility are discussed in Section 5. The transfer functions and mode shapes are obtained from the FE model. For verification, a scanning laser vibrometer is used to measure the corresponding operational deflection shapes. Milling tests at different clamping torques are conducted to study the chatter stability. The conclusions are given in the last section.

2 Modeling of spindle system and micro-end mill

2.1 Coordinate systems

The micro-milling machine tool (WISSNER Gamma 303 HP 3-axis) is described by the inertial (fixed) Cartesian reference frame $\mathscr{N}$ with coordinates x, y, and z, as shown in Fig. 1. The coordinate x is set to be coincident with the rotational direction of the spindle, which is usually in the clockwise direction (top view). The milling plane is described with coordinates y and z, where y denotes the feed direction and z denotes the lateral direction.

In order to describe the kinematics of the rotating bodies, a reference frame $\mathscr{T}$ with coordinates $\tilde{x}$, $\tilde{y}$, and $\tilde{z}$ is attached on the centerline of the rotor with the $\tilde{x}$-axis normal to the cross-section. The direction cosine matrix between $\mathscr{N}$ and $\mathscr{T}$ is defined by introducing two intermediate frames as well as three successive rotations as follows:

1. α about y defining the first intermediate frame with coordinates x_1, y_1, and z_1,
2. β about z_1 defining the second intermediate frame with coordinates x_2, y_2, and z_2,
3. γ about x_2 defining the body-attached frame with coordinates $\tilde{x}$, $\tilde{y}$, and $\tilde{z}$.

Accordingly, the position vector of the cross-section in $\mathscr{N}$ is defined by two transverse translations in

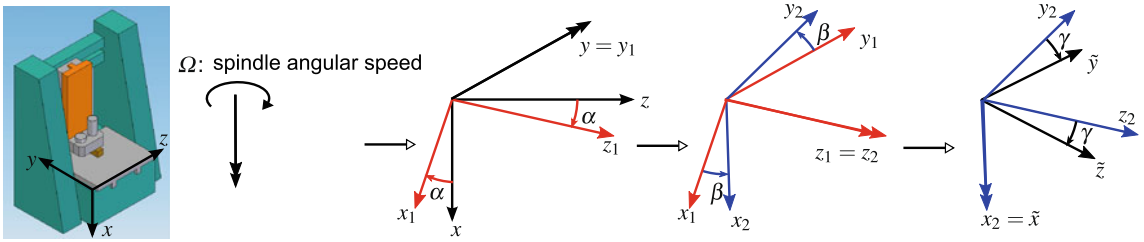

Fig. 1 Coordinate systems for the description of rotating bodies

accordance with z- and $y(= y_1)$-directions, respectively. It is assumed that a nonholonomic constraint

$$^{\mathcal{N}}\boldsymbol{\omega}^{\mathcal{T}} \cdot \mathbf{e}_x = \Omega \tag{1}$$

holds, where $^{\mathcal{N}}\boldsymbol{\omega}^{\mathcal{T}}$ is the angular velocity vector with respect to the inertial system and Ω is the constant spindle speed in rad s^{-1}.

A second option to describe the direction cosine matrix between the reference frames $\mathcal{N}$ and $\mathcal{T}$ is, e.g., changing the rotational sequence as follows:

1. γ about x defining the first intermediate frame with coordinates $\hat{x}$, $\hat{y}$, and $\hat{z}$, i.e., the rotating frame $\mathcal{S}$,
2. α about $\hat{y}$ defining the second intermediate frame with coordinates $\hat{x}_1$, $\hat{y}_1$, and $\hat{z}_1$,
3. β about $\hat{z}_1$ defining the body-attached frame with coordinates $\tilde{x}$, $\tilde{y}$, and $\tilde{z}$.

Accordingly, the position vector of the cross-section in $\mathcal{N}$ is defined by two transverse translations in accordance with $\hat{z}$- and $\hat{y}(= \hat{y}_1)$-directions, respectively, and the same nonholonomic constraint (Eq. 1) remains.

In the following, the equations of motion are first derived using the first option, i.e., with respect to the inertial frame $\mathcal{N}$. The linearized equations with respect to the rotating frame $\mathcal{S}$ (quasi body-attached frame[1]) are then obtained with the help of an orthogonal transformation matrix. Both forms of dynamical equations are compared with each other.

2.2 Element equations of motion

Figure 2 illustrates the studied spindle system (with rotational speeds from 10,000 to 60,000 rpm), a micro-end mill, and a beam element. The characterized geometric parameters of the micro-end mill are the shank length l_s, the shank diameter d_s, the taper length l_c, the tip length l_t, and the nominal tip diameter d_t. The taper section possesses a varying radius along the beam axis and is discretized by a series of uniform beam elements. The radius of each element is approximated by the radius of the medium cross-section. The fluted part of the micro-end mill is regarded as circular cross-section with an effective diameter $0.8d_t$. The spindle shaft features a hollow circular cross-section and a tapered segment at the front in order to match the tool holder. It can be treated as four sections, three of which have constant outer and inner radii. The taper section has a constant outer radius and a varying inner radius and can be discretized by uniform beam elements with constant cross-sections. The tool holder (ATC 2-10-6) inclusive the collet (SRP 6) can be approximated by a taper section that is combined with the spindle shaft and a uniform section outside the spindle shaft. The inner radius of the tool holder (inclusive collet) is assumed to be the same as the shank radius of the tool.

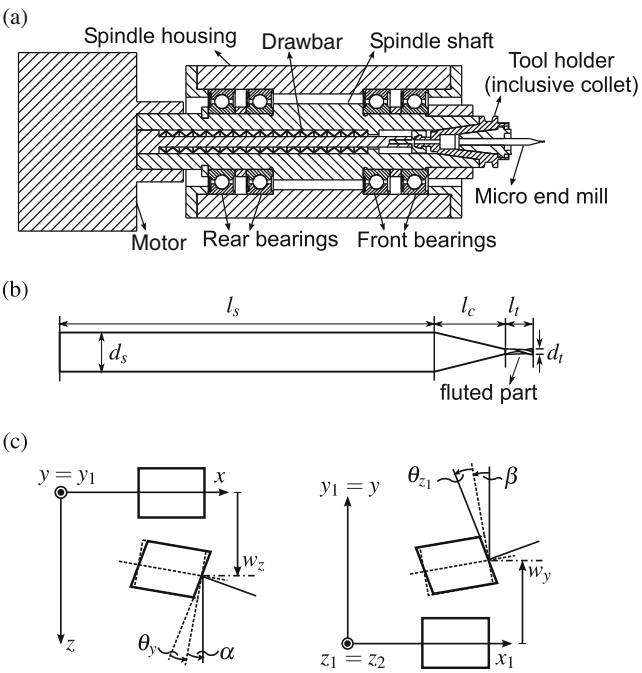

Fig. 2 Schematics of **a** the spindle system Fischer Precise SC 3062, **b** a micro-end mill, and **c** Timoshenko beam element

[1]By linearization of small bending angles, the quasi body-attached frame can be approximated to the body-attached frame.

Since micro-end mills are usually employed with relatively short free shank length, the Timoshenko beam theory is adopted to incorporate the shear deformation. The angular deflections due to bending are α and β which are consistent with the rotating angles. The angular deflections due to shear are denoted by θ_y and θ_{z_1}. Since these rotation angles are small, the slopes of the beam can be linearized with respect to the axes x, x_1, and $\tilde{x}$, which leads to the following relations

$$w'_z(\tilde{x},t) = \frac{\partial}{\partial \tilde{x}} w_z(\tilde{x},t) \approx \frac{\partial}{\partial x} w_z(x,t) = -\alpha(x,t) - \theta_y(x,t), \tag{2}$$

$$w'_y(\tilde{x},t) = \frac{\partial}{\partial \tilde{x}} w_y(\tilde{x},t) \approx \frac{\partial}{\partial x_1} w_y(x_1,t) = \beta(x_1,t) + \theta_{z_1}(x_1,t). \tag{3}$$

A simple beam element, which has two nodes and four degrees of freedom (two transverse translations and two rotations) at each node, is used here for a circular and uniform cross-section [28]. The axial and torsional displacements are neglected because the rigidity of the milling system with respect to these directions is higher compared to that of the transverse directions. In order to express the element, time-dependent generalized coordinates

$$\mathbf{q}^e(t) = \left(q_1^e(t), q_2^e(t), q_3^e(t), q_4^e(t), q_5^e(t), q_6^e(t), q_7^e(t), q_8^e(t)\right)^{\mathsf{T}} \tag{4}$$

are defined. The translational displacements q_1^e and q_3^e at the start node as well as q_5^e and q_7^e at the end node are in the same directions of the unit vectors $\mathbf{e}_z$ and $\mathbf{e}_y$, respectively. The rotational displacements q_2^e and q_4^e at the start node as well as q_6^e and q_8^e at the end node are rotating angles about the y-axis and the z_1-axis, respectively, which are consistent with the bending angles. Neglecting the axial and torsional displacements, the translations and the rotations of an arbitrary point on the beam axis can be expressed as

$$\begin{pmatrix} w_z(s,t) \\ w_y(s,t) \end{pmatrix} = \mathbf{\Psi}(s)\mathbf{q}^e(t), \qquad \begin{pmatrix} \alpha(s,t) \\ \beta(s,t) \end{pmatrix} = \mathbf{\Phi}(s)\mathbf{q}^e(t), \tag{5}$$

where s denotes the local coordinate of the beam element and the shape functions $\mathbf{\Psi}$ (for the translations) and $\mathbf{\Phi}$ (for the bending angles), considering both bending and shear deformations can be found in [28].

The equations of motion of the beam element can be derived using Hamilton's principle:

$$\delta \int_{t_1}^{t_2} \left(T^e - U^e\right) \mathrm{d}t + \int_{t_1}^{t_2} \delta W^e \mathrm{d}t = 0, \tag{6}$$

where δ represents the variational operator, T^e and U^e are the kinetic and potential energy of the beam element, respectively, and δW^e is the virtual work of the nonconservative forces. The total kinetic energy is composed of translational and rotational parts and can be expressed as

$$T^e = \frac{1}{2}\int_0^l \mu\left(\dot{w}_z^2 + \dot{w}_y^2\right) \mathrm{d}s + \frac{1}{2}\int_0^l \left(\Theta_{\tilde{x}}\omega_1^2 + \Theta_{\tilde{y}}\omega_2^2 + \Theta_{\tilde{z}}\omega_3^2\right) \mathrm{d}s. \tag{7}$$

Here, μ is the mass per unit length. $\dot{w}_y$ and $\dot{w}_z$ are the components of the absolute translational velocity with respect to the inertial frame. ω_1, ω_2, and ω_3 are the components of the angular velocity in the body-attached frame. $\Theta_{\tilde{x}}$, $\Theta_{\tilde{y}}$, and $\Theta_{\tilde{z}}$ are the components of the moment of inertia with respect to the principal axes. Note that the diametral terms $\Theta_{\tilde{y}}$ and $\Theta_{\tilde{z}}$ are the same for a circular cross-section and equal to the half value of $\Theta_{\tilde{x}}$.

Neglecting the torsional deformation and the axial load, the total potential energy consists of the energy due to bending and shear deformations. Using Eqs. 2 and 3, in which the coordinate $\tilde{x}$ is replaced by the coordinate s, it can be described as

$$U^e = \frac{1}{2}\int_0^l EI\left(\left(\alpha'\right)^2 + \left(\beta'\right)^2\right) \mathrm{d}s + \frac{1}{2}\int_0^l \kappa GA\left(\left(-w'_z - \alpha\right)^2 + \left(w'_y - \beta\right)^2\right) \mathrm{d}s. \tag{8}$$

The virtual work on the beam element δW^e results from the nonconservative forces due to external loads and external as well as internal damping. For the element equations, the damping effect is first excluded. It will be implemented later into the assembled equations.

Expressing the translations and rotations by the nodal coordinates $\mathbf{q}^e$ and considering the nonholonomic constraint (see Eq. 1), the equations of motion of the beam element can be derived with the help of variational calculation. The linearized form is given by

$$\mathbf{M}^e\ddot{\mathbf{q}}^e - \Omega\mathbf{G}^e\dot{\mathbf{q}}^e + \mathbf{K}^e\mathbf{q}^e = \mathbf{f}^e, \tag{9}$$

where $\mathbf{f}^e$ denotes the external loads (cutting forces) that act on the corresponding nodes. The structural matrices in this equation are time-independent since uniform circular cross-sections are assumed. The symmetric mass matrix $\mathbf{M}^e$ due to translational and rotational inertia is

$$\mathbf{M}^e = \mathbf{M}_t^e + \mathbf{M}_r^e = \int_0^l \mu\mathbf{\Psi}^{\mathsf{T}}\mathbf{\Psi}\mathrm{d}s + \int_0^l \frac{\mu r^2}{4}\mathbf{\Phi}^{\mathsf{T}}\mathbf{\Phi}\mathrm{d}s, \tag{10}$$

where r denotes the radius of the beam element. The skew-symmetric matrix $\mathbf{G}^e$ is

$$\mathbf{G}^e = \int_0^l \frac{\mu r^2}{2} \mathbf{\Phi}^{\mathsf{T}} \begin{bmatrix} 0 & -1 \\ 1 & 0 \end{bmatrix} \mathbf{\Phi} \mathrm{d}s = 2\mathbf{M}_r^e \mathbf{S}^e \tag{11}$$

with

$$\boldsymbol{S}^e = \begin{bmatrix} 0 & 0 & 1 & 0 & 0 & 0 & 0 & 0 \\ 0 & 0 & 0 & -1 & 0 & 0 & 0 & 0 \\ -1 & 0 & 0 & 0 & 0 & 0 & 0 & 0 \\ 0 & 1 & 0 & 0 & 0 & 0 & 0 & 0 \\ 0 & 0 & 0 & 0 & 0 & 0 & 1 & 0 \\ 0 & 0 & 0 & 0 & 0 & 0 & 0 & -1 \\ 0 & 0 & 0 & 0 & -1 & 0 & 0 & 0 \\ 0 & 0 & 0 & 0 & 0 & 1 & 0 & 0 \end{bmatrix}. \tag{12}$$

The symmetric stiffness matrix $\mathbf{K}^e$ due to bending and shear is

$$\mathbf{K}^e = \mathbf{K}_b^e + \mathbf{K}_s^e = \int_0^l EI \mathbf{\Phi}'^{\mathsf{T}} \mathbf{\Phi}' \mathrm{d}s + \int_0^l \kappa GA \left(\begin{bmatrix} -\mathbf{\Psi}'_z \\ \mathbf{\Psi}'_y \end{bmatrix} - \mathbf{\Phi} \right)^{\mathsf{T}} \left(\begin{bmatrix} -\mathbf{\Psi}'_z \\ \mathbf{\Psi}'_y \end{bmatrix} - \mathbf{\Phi} \right) \mathrm{d}s \tag{13}$$

with

$$\mathbf{\Psi}' = \begin{bmatrix} \mathbf{\Psi}'_z \\ \mathbf{\Psi}'_y \end{bmatrix}. \tag{14}$$

The equations of motion can be derived in the rotating frame in the same way. For the linearized equations, a simplified and more convenient transformation can be employed with the help of an auxiliary rotation matrix $\mathbf{R}^e$ (orthogonal transformation matrix consisting of terms $\cos \Omega t$ and $\sin \Omega t$) [28]. The relation between $\mathbf{q}^e$ with respect to the inertial frame and $\hat{\mathbf{q}}^e$ with respect to the rotating frame can be given by

$$\mathbf{q}^e = \mathbf{R}^e \hat{\mathbf{q}}^e. \tag{15}$$

Substituting this equation and the derivatives into Eq. 9 and premultiplying by $\mathbf{R}^{e\mathsf{T}}$ yields

$$\mathbf{M}^e \ddot{\hat{\mathbf{q}}}^e + \left(2\Omega \hat{\mathbf{M}}^e - \Omega \mathbf{G}^e \right) \dot{\hat{\mathbf{q}}}^e + \left(\mathbf{K}^e - \Omega^2 \left(\mathbf{M}^e + \hat{\mathbf{G}}^e \right) \right) \hat{\mathbf{q}}^e = \hat{\mathbf{f}}^e, \tag{16}$$

where the skew-symmetric matrix $\hat{\mathbf{M}}^e$ that consists of the translational and rotational parts is

$$\hat{\mathbf{M}}^e = \mathbf{M}^e \mathbf{S}^e = \left(\mathbf{M}_t^e + \mathbf{M}_r^e \right) \mathbf{S}^e = \hat{\mathbf{M}}_t^e + \frac{1}{2} \mathbf{G}^e \tag{17}$$

and the symmetric matrix $\hat{\mathbf{G}}^e$ is

$$\hat{\mathbf{G}}^e = \mathbf{G}^e \mathbf{S}^e = 2\mathbf{M}_r^e \mathbf{S}^e \mathbf{S}^e = -2\mathbf{M}_r^e. \tag{18}$$

Thus, Eq. 16 can be reduced to

$$\mathbf{M}^e \ddot{\hat{\mathbf{q}}}^e + 2\Omega \hat{\mathbf{M}}_t^e \dot{\hat{\mathbf{q}}}^e + \left(\mathbf{K}^e - \Omega^2 \left(\mathbf{M}_t^e - \mathbf{M}_r^e \right) \right) \hat{\mathbf{q}}^e = \hat{\mathbf{f}}^e. \tag{19}$$

Comparing Eqs. 9 and 19, the following main differences can be stated:

- With respect to the inertial frame, the deduced gyroscopic terms ($-\Omega \mathbf{G}^e$) result from the rotational inertia of the beam element. With respect to the rotating frame, they ($2\Omega \hat{\mathbf{M}}_t^e$) result from the translational inertia.
- In the rotating frame, the terms $-\Omega^2 \mathbf{M}_t^e$ and $\Omega^2 \mathbf{M}_r^e$ due to the translational and rotational inertia, respectively, appear with opposite signs in the displacement proportional matrices of Eq. 19.

Due to the presence of the gyroscopic terms, the natural frequencies of the system are split into backward and forward ones (whirl speeds). The frequency values calculated with respect to the rotating frame differ from those with respect to the inertial frame. More precisely, the differences result from the angular frequency of the rotating shaft.

It should be mentioned that the torsion and compression–tension effects are not included in the beam model. For various designs, the mode due to torsional deformation could have a lower natural frequency compared to the higher bending modes [22, 23].

2.3 Assembled equations of motion

The system's equations of motion can be derived by assembling the equations of all elements considering the clamping conditions at the STT interfaces. The behavior of the STT joints is usually nonlinear and anisotropic for various system designs [10]. It is challenging to accurately identify the contact properties for each interface node of the FE model. Especially, the actual contact mechanism at the tool holder–tool joint is difficult to identify. Owing to the slots that are fabricated in the collet, the positions of the contact nodes are difficult to define. The stiffness and damping properties at diverse contact positions and directions could be different. In order to simplify the modeling, it is assumed that the tool holder–tool joint is approximated by single-node coupling at the built-in point. The tool shank part that is connected to the collet is rigidly coupled to the tool holder. The spindle–tool holder joint is modeled with distributed multinodes. The nodal displacements are constrained through translational and rotational springs with linear stiffness and damping. Since the spindle bearings (FAG XCB7004-C-T-P4S) do not transmit torque, they are

modeled as translational springs and dampers only. Clearance effects are neglected.

To introduce a linear form of damping, one possibility is the application of Rayleigh damping. The stiffness proportional part intensively damps the higher vibration modes, while the lower modes are mainly affected by the mass proportional part. Another possibility is the use of the damping ratios for individual modes. The backward calculation from the modal space can be expressed as

$$\mathbf{D} = \left(\varphi^{\mathsf{T}}\right)^{-1} \left(2\sigma_0 \varpi_0\right) \varphi^{-1}, \tag{20}$$

where $\mathbf{D}$ is the spatial damping matrix, φ is the normalized eigenvector matrix, σ_0 is the diagonal damping ratio matrix, and ϖ_0 is the diagonal natural frequency matrix. It should be noted that this evaluation is valid for proportional damping but not for general viscous damping [29]. Using this symmetric damping matrix $\mathbf{D}$, the assembled dynamical equation with respect to the inertial frame can be given by

$$\mathbf{M}\ddot{\mathbf{q}} + (\mathbf{D} - \Omega\mathbf{G})\,\dot{\mathbf{q}} + \mathbf{K}\mathbf{q} = \mathbf{f}. \tag{21}$$

Here, $\mathbf{q}$ denotes the generalized coordinates of the assembly and $\mathbf{f}$ denotes the external loads. The matrices $\mathbf{M}$, $\mathbf{G}$, and $\mathbf{K}$ can be obtained by arranging the element matrices, respectively.

According to that, the linear equation with respect to the rotating frame is given by

$$\mathbf{M}\ddot{\hat{\mathbf{q}}} + \left(\mathbf{D} + 2\Omega\hat{\mathbf{M}}_t\right)\dot{\hat{\mathbf{q}}} + \left(\mathbf{K} - \Omega^2\left(\mathbf{M}_t - \mathbf{M}_r\right) + \Omega\hat{\mathbf{D}}\right)\hat{\mathbf{q}} = \hat{\mathbf{f}}. \tag{22}$$

Here, $\hat{\mathbf{q}}$ and $\hat{\mathbf{f}}$ denote the displacements and forces with respect to the rotating frame, respectively. Since the symmetric damping matrix $\mathbf{D}$ is assumed with respect to the inertial frame, a skew-symmetric matrix $\Omega\hat{\mathbf{D}}$ arises with respect to the rotating frame. In case of light damping, this matrix has no significant effect on the system dynamics. It should be pointed out that the restoring forces of the springs are assumed to be parallel to the two mutual perpendicular axes of the reference frame while assembling the dynamical equations, i.e., they are always centrally directed to the origin of the reference frame.

2.4 Parameter estimation

The material properties of the cemented carbide micro-end mills are given in [30] (Young's modulus, 640 GPa; density, 14,900 kg m^{-3}; and Poisson's ratio, 0.22). The corresponding data of the spindle shaft and tool holder are 210 GPa, 7,874 kg m^{-3}, and 0.3.

Table 1 Translational stiffness of the spindle–tool holder–tool interfaces and the bearings (SC 3062)

Translational stiffness	Value (Nm^{-1})
k^b (from FAG)	1.89×10^7
k_t^{sh} (from Fischer Precise)	2.8×10^7
k_t^{ht} (single-node coupling)	3.36×10^6

The translational stiffness k_t^{sh} at the spindle–tool holder joint is estimated from the radial stiffness at the top of the spindle. The stiffness of the ceramic bearing balls k_t^b is assumed to be isotropic. Their values can be obtained based on the data sheet of FAG and Fischer Precise. The translational stiffness k_t^{th} between the tool holder and tool can be identified by transfer functions measured at the tool tip [31, 32] or the mode-dependent chatter frequency [12]. The identified values for a clamping torque of 12 Nm are given in Table 1. In addition, it is difficult to measure the tool tip transfer function in micro-cutting by conventional experimental modal analysis. In the next section, a new method using piezoelectric elements is presented. The transfer behavior in the operating state can be identified.

The rotational stiffness values at the spindle–tool holder (k_r^{sh}) and tool holder–tool (k_r^{th}), respectively, are assumed to be the same as the corresponding translational stiffness values. The rationality of this assumption, i.e., the sensitivity of the rotational and translational stiffness, is discussed later with numerical results in Section 5.2. As stated in [10, 14], the damping also depends on the clamping forces/torques and the drawbar forces. Their estimation is much more difficult in contrast to the stiffness estimation. In order to reduce the complexity, damping values of all interfaces are adjusted to ensure the magnitudes of the transfer functions in the reasonable range, especially for the dominant modes.

3 Identification of transfer behavior using piezoelectric elements

Usually, the conventional experimental modal analysis cannot be applied to a rotating system. The small sizes of the micro-cutting tools also enlarge the difficulty of identification of transfer functions. Piezoelectric materials provide a possible and an efficient way. Using the piezoceramic staple actuators, "smart pads" are manufactured to study the squeal behavior of disk brakes in the operating state [24–27]. By additional accelerometer and/or laser vibrometer, the transfer functions of the rotating system were identified. Furthermore, the

squealing frequency was also successfully detected before the actual squeal occurred.

Similarly, a "smart workpiece" can be developed by integrating the piezoelectric staple elements into the chuck system, as shown in Fig. 3a. Two two-layer piezoelements are clamped between the workpiece and the chuck system. During the cutting operations, the piezoelements are used as actuators, i.e., excited by the external signals that should have a wide frequency bandwidth. The velocity of the tool shank point is measured by the laser vibrometer. Thus, the transfer behavior of the micro-end mill in the operating (rotating) state can be identified.

Figure 3b depicts the result that is achieved using random noise as external excitations (with the amplitude of 100 V). The transfer function is described by velocity/voltage at a spindle speed of 29,000 rpm and an axial depth of cut of 55 μm. The striking peak with the highest magnitude corresponds to the dominant mode of the system. Due to the rotation of the two-edge cutting tool, the spindle frequency, the cutting edge engagement frequency, and their harmonics are also detected, but they reveal quite low magnitudes. Other frequencies in the resonance range are approximately

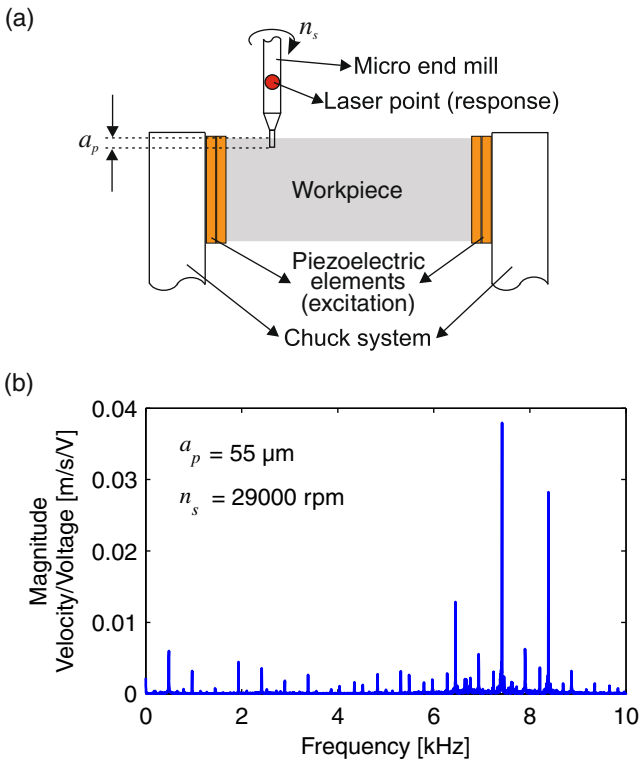

Fig. 3 Identification of transfer functions using piezoelectric actuators. **a** Experimental setup and **b** transfer function using random noise as excitation on a micro-end mill with tool tip diameter of $d_t = 1$ mm (workpiece material: CuZn39Pb1)

equal to the combination of the dominant frequency and the harmonics. It should be noted that slotting operations are adopted here. For low radial immersions, the detected dominant frequency may be equal to half of the cutting frequency since the period doubling instability can arise in that case.

4 Gyroscopic effect

4.1 Dynamics in the inertial and rotating frames

At the rotating state, the equations of motion cannot be decoupled in two orthogonal directions of the milling plane. Due to the gyroscopic terms, the natural frequencies of the system are split into backward and forward ones. The cross-transfer functions take effect due to the angular velocity of the spindle. Since the linear equations are derived in the inertial and rotating frames, the rotational effects are studied for both cases.

With respect to the inertial frame (see Eq. 21), the gyroscopic matrix results from the rotary inertia, i.e., $-\Omega\mathbf{G} = -2\Omega\hat{\mathbf{M}}_r$. Figure 4a shows the direct (FRF_{yy}) and the cross-transfer (FRF_{zy}) functions with excitation and response at the tool tip at a rotational speed of 60,000 rpm. The peak-splitting effect of the dominant modes cannot be distinctly observed. With respect to the rotating frame (see Eq. 22), the gyroscopic matrix results from the translational inertia ($2\Omega\hat{\mathbf{M}}_t$). With the same parameters as in the inertial frame, the peak-splitting effect is distinctly observed from the dominant modes of both direct and cross tool tip transfer functions, as shown in Fig. 4b.

Figure 4c, d illustrates the change of backward and forward frequencies of the first dominant mode with spindle speeds in the two frames. It is clear that the mode-splitting effect in the rotating frame is much more significant. Table 2 gives the corresponding natural frequencies of the first three dominant modes at the nonrotating and rotating states in the inertial frame. The frequencies of each mode at 60,000 rpm differ from each other to such an extent that they cannot be distinguished from the transfer functions.

Note that the corresponding whirl speeds in Fig. 4d are computed within the frame that rotates with an angular speed Ω relatively to the inertial frame. When the whirl speeds are expressed with respect to the inertial frame, i.e., adding or subtracting the rotational frequency, respectively, to the backward one or from the forward one, they should be identical to those computed with respect to the inertial frame. To demonstrate this, the first dominant mode is taken as an example. The whirl speeds in the rotating frame are

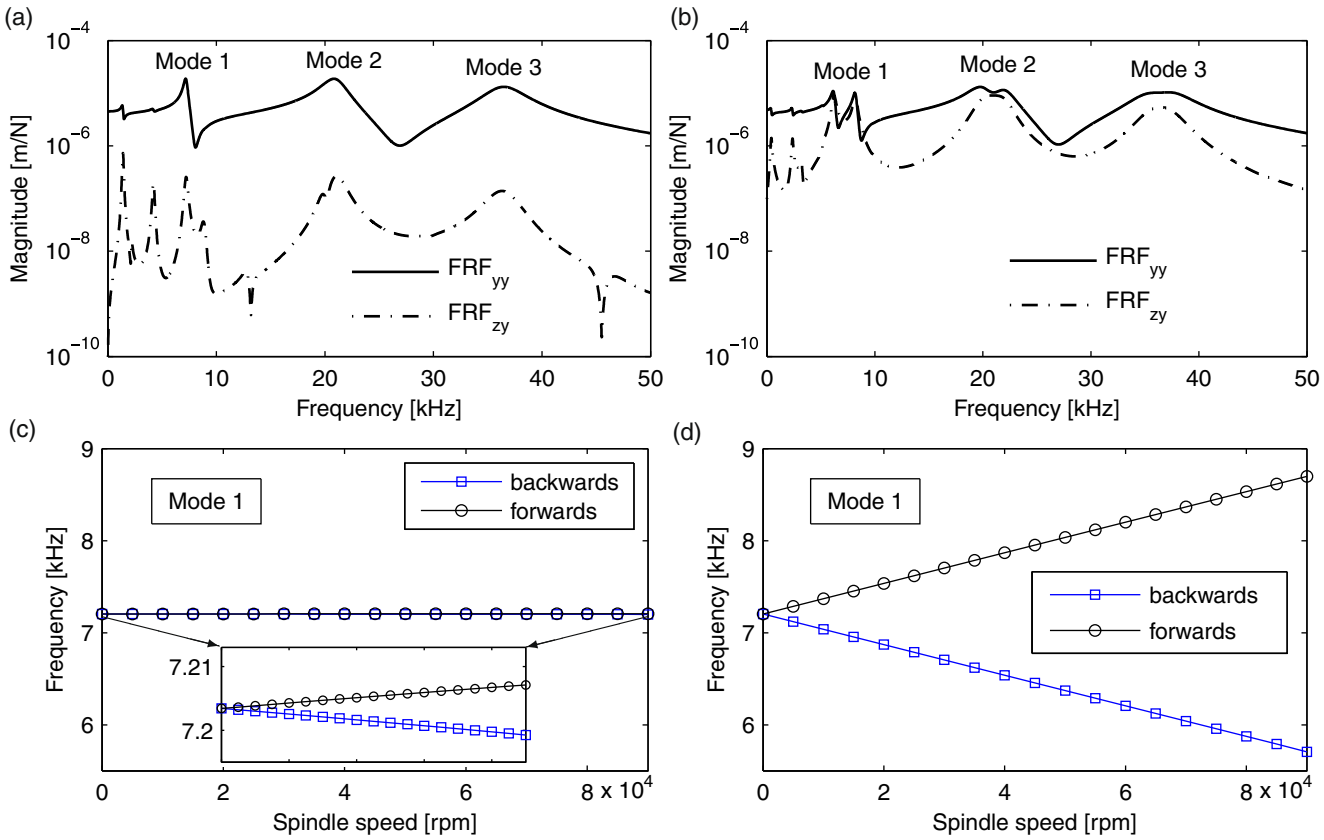

Fig. 4 Gyroscopic effect on the dynamics of direct (FRF_{yy}) and cross-transfer (FRF_{zy}) functions at the tool tip in **a** the inertial frame and **b** the rotating frame at a spindle speed of 60,000 rpm; backward and forward frequencies of the first dominant mode in **c** the inertial frame and **d** the rotating frame

6.206–8.201 kHz. Taking into account the rotational frequency (1 kHz), the whirl speeds in the inertial frame are 7.206 and 7.201 kHz, respectively, which equal the values of the first dominant mode in Table 2.

If the gyroscopic terms due to the translational inertia $2\hat{\mathbf{M}}_t$ in Eq. 22 are omitted, the corresponding frequencies of the first dominant mode at 60,000 rpm are almost the same, i.e., 7.131 and 7.137 kHz, respectively. Compared to the value (7.203 kHz) at the nonrorating state, the decrease results from the terms $-\Omega^2(\mathbf{M}_t - \mathbf{M}_r)$. In addition, as a result of the relatively small damping ratios, the skew-symmetric matrix $-\Omega\hat{\mathbf{D}}$ has no significant effect on the system dynamics.

The results above reveal that the gyroscopic effect on the tool tip transfer functions calculated in the rotating frame cannot be neglected. They also indicate that in micro-milling, the contribution of the translational inertia to the gyroscopic effect is much more important than that of the rotary inertia. The radii of micro-end mills lie in the ranges of millimeter (shank) and micrometer (tip). Compared to the translational inertia, the rotational inertia of a finite element is proportional to the square of the radius, which sharply reduces the corresponding values of the skew-symmetric matrix that is proportional to the velocity.

Table 2 The first three dominant natural frequencies of the spindle system (SC 3062) at 0 and 60,000 rpm in the inertial frame

Dominant mode (rpm)	1 (kHz)	2 (kHz)	3 (kHz)
0	7.203	20.970	36.430
60,000 (backward)	7.201	20.953	36.410
60,000 (forward)	7.206	20.988	36.450

4.2 Chatter stability in the inertial frame

The chatter behavior can be characterized by the chatter frequencies that are usually experimentally detected with respect to the inertial frame. Thus, the dynamical equation (see Eq. 21) derived in the inertial frame is used to compare the analytical and experimental results. The cutting mechanism in micro-milling is more complicated than that in conventional milling (e.g., the minimum chip thickness effect [4–6]). Here, the feed per tooth is chosen at 10 μm so that the shearing dominates and the conventional milling force models (e.g.,

according to Altintas [33]) can be applied [1, 11]. In this case, Eq. 21 can be modified to the following delay differential equation (DDE)

$$\mathbf{M}\ddot{\mathbf{q}}(t) + (\mathbf{D} - \Omega\mathbf{G})\,\dot{\mathbf{q}}(t) + \mathbf{K}\mathbf{q}(t) = a_p K_t \mathbf{A}(t)\left(\mathbf{q}(t) - \mathbf{q}(t-T)\right), \quad (23)$$

where T is the cutting period, a_p is the axial depth of cut, K_t is the cutting force coefficient in the tangential direction, and $\boldsymbol{A}(t)$ contains the directional force matrix as well as the radial to tangential force ratio k_{co}. The frequencies involved in the periodic coefficient $\boldsymbol{A}(t)$ depend on the entry and exit angles of the cutting process, i.e., the ratio of the radial depth of cut to tool tip diameter. The methods in the frequency domain according to Altintas and Budak [33, 34] are employed for chatter stability prediction.

Note that the dynamics of the workpiece system is not included in this paper. In order to focus on the spindle and micro-cutting tools, workpieces without thin walls are used and stiffly clamped into the chuck system so that their dynamics can be neglected compared to the micro-end mill dynamics.

Figure 5 shows the analytical stability boundaries and the experimental results that are determined by the chatter frequencies of the acoustic signals. It can be seen that the analytical boundaries with and without gyroscopic effect are almost the same and in accordance with the experimental results. This is not surprising since the tool tip dynamics with respect to the inertial frame is not strongly affected by the gyroscopic effect, as stated in Section 4.1. The process stability depends on the dominant modes which are mainly caused by the deflections of the micro-end mill. Due to its small rotary inertia, the gyroscopic effect is reduced in spite of the high rotational velocity. Compared to conventional high-speed machining, the mode-splitting effect and the gyroscopic effect observed in the inertial frame are negligible for chatter stability in micro-milling. The discrepancies between the analytical and experimental results could result from the variation of the force coefficients that are not considered in the analytical solutions. For a conservative chatter prediction, the robust stability analysis can be employed [35].

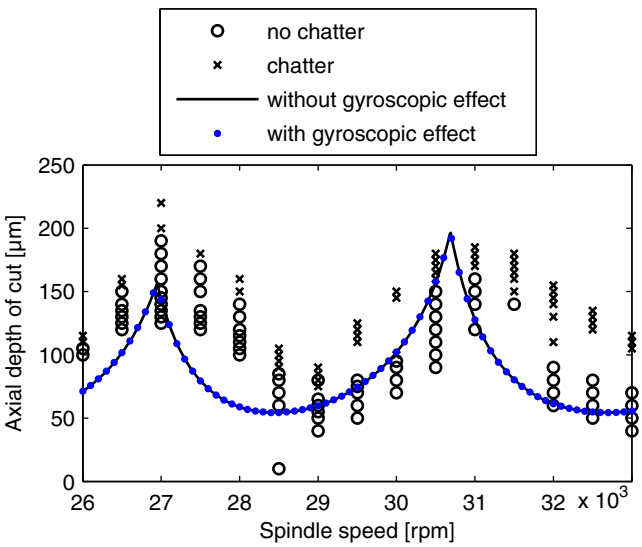

Fig. 5 Analytical (with and without gyroscopic effect) and experimental chatter charts

5 Effects of mode interaction and joint flexibility

5.1 Dynamics in the inertial frame

According to the analysis in Section 4, the gyroscopic effect can be neglected in the inertial frame. Hence, the spindle system and subsystems are analyzed at the nonrotating state ($\Omega = 0$) to study the effects of the mode interaction and joint flexibility. The transfer functions of the micro-end mill under ideally clamped–free boundary conditions (T), the spindle, the spindle–tool holder by rigid coupling, and the entire system (STT) are compared with each other. The top panel of Fig. 6 illustrates transfer functions in y-direction of the milling plane, which are calculated with both excitation and response at the end node (tip point) of the corresponding systems. It can be seen that the magnitudes of the tip receptance of the cantilever tool are much higher than that of the spindle. Owing to nonrigid modeling of the spindle bearings, the first two deformation shapes of the spindle arise from the constraint modes, i.e., the rigid body motions. Coupling the spindle with the tool holder rigidly, the receptance at the end node of the tool holder is shifted, but no significant change of the magnitudes can be observed.

After coupling the micro-end mill to the tool holder, the tip dynamics of the spindle system is significantly altered. The magnitudes of the receptance increase to a large extent because of the more flexible tool. Moreover, the two dominant frequencies f_{T1} (13.831 kHz) and f_{T2} (32.141 kHz) of the cantilever tool are greatly shifted by elastic coupling to f_{STT1} (20.970 kHz) and f_{STT2} (36.430 kHz). The modes of the spindle or spindle–tool holder are depressed, which can be exhibited from the small peaks of the system receptance. Interestingly, a dominant frequency f_{STT0} (7.203 kHz) arises due to the interactions between the modes of the spindle and the tool.

The middle and bottom panels in Fig. 6 show the corresponding normalized mode shapes that are calculated

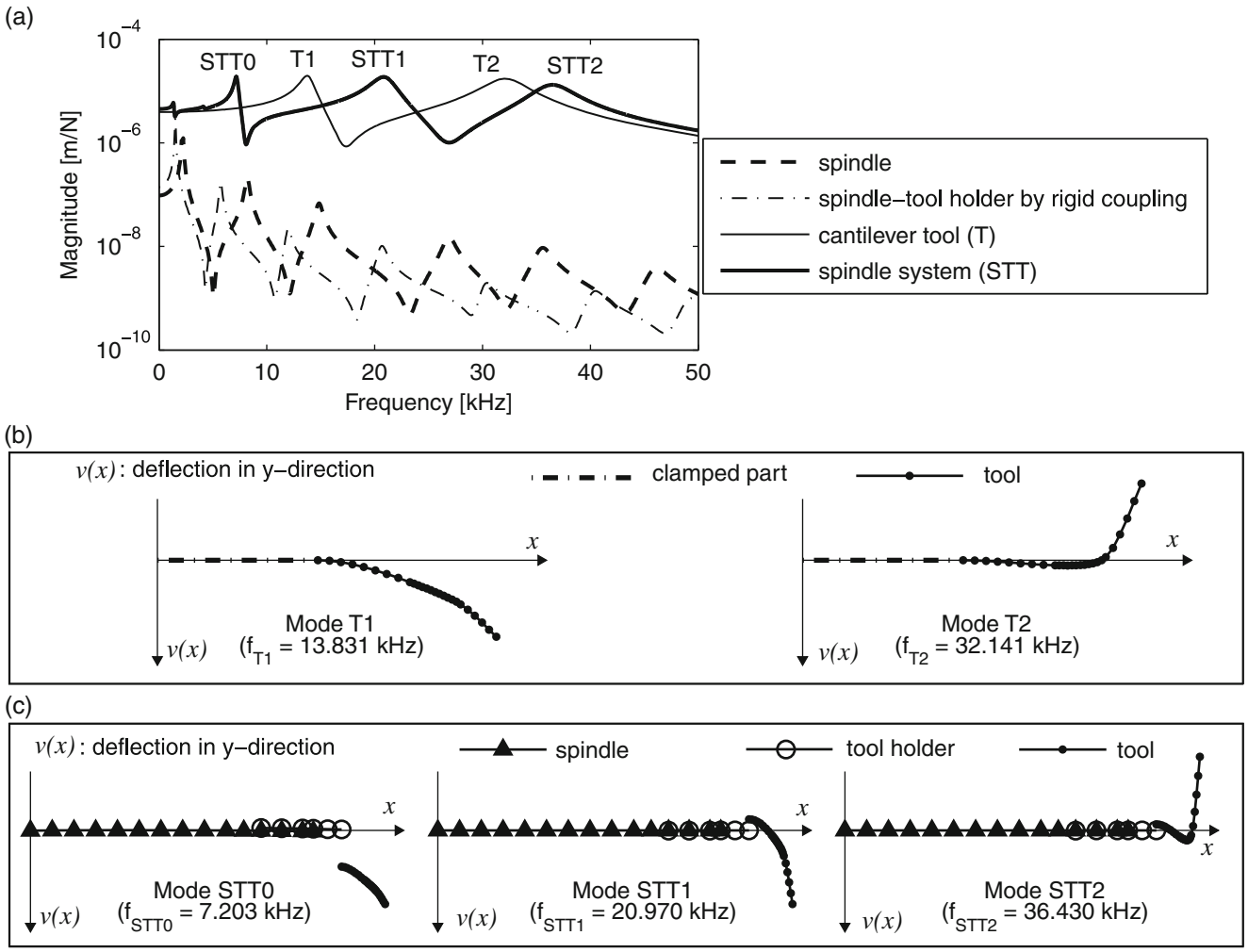

Fig. 6 Mode interaction effect on the dynamics **a** of transfer functions at the end node (tip point) of the cantilever tool (T), the spindle, the spindle–tool holder by rigid coupling, and the spindle system (STT); **b** of mode shapes of the cantilever tool (T); **c** of mode shapes of the spindle system (STT)

from the eigenvectors for the cantilever tool and the spindle system. All deflection shapes reflect that the micro-end mill, especially the tip section, is the most flexible part. For the dominant mode STT0, the tool exhibits a combination of rigid body motions and bending deflections, while the spindle and the tool holder reveal almost no deformations at this mode. Due to the design of the micro-end mills, the machine tool dynamics in micro-milling is more significantly influenced by the micro-end mill compared to conventional milling setups.

This mode interaction effect is experimentally validated with the help of the scanning laser vibrometer. The operational deflection shapes at the chatter frequencies can be identified. Owing to the quite short operating time, three points on the shank of the micro-end mill are measured. The points on the taper and tip sections cannot provide sufficient reflection signals. The results are demonstrated in Fig. 7, where the corresponding mode shapes of the FE model are computed by the eigenvectors.

Figure 7a shows an operational deflection shape (for a micro-end mill with tip diameter of $d_t = 0.5\,\text{mm}$) identified by the scanning laser vibrometer in an inclined direction of the milling plane. Figure 7b depicts the deflection shapes identified by experiments for $d_t = 0.5\,\text{mm}$ and $d_t = 0.2\,\text{mm}$ in the feed direction, while Fig. 7c gives the corresponding mode shapes computed by analytical models. It can be seen that the micro-end mills in both cases cannot be treated as perfect cantilever beam. This bending mode is primarily caused by the tool shank. Since the difference of the shank length for both cases is small (34.7 and 35.3 mm, respectively), the computed results reveal almost the same mode shapes. It can be seen that the chatter frequencies are located in the resonance range and can differ from

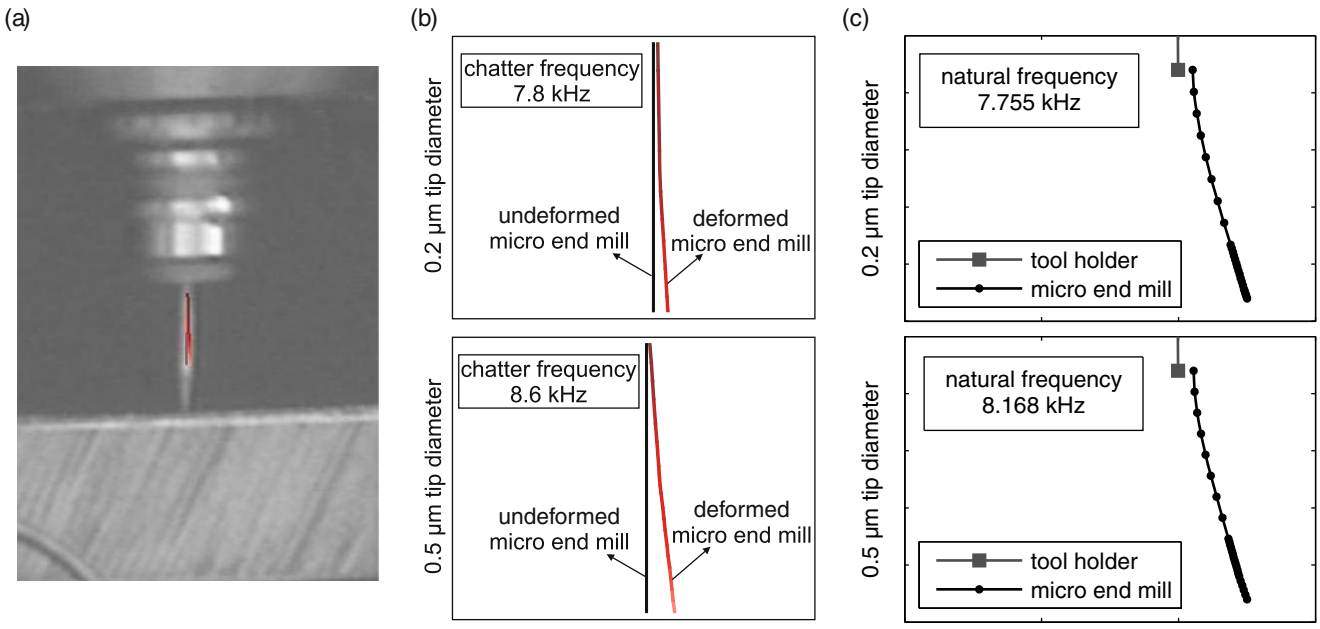

Fig. 7 Operational deflection shapes identified by the scanning laser vibrometer. **a** In inclined direction. **b** Feed direction of the milling plane. **c** Computed mode shapes in feed direction

the natural frequency to some degree (e.g., the case of $d_t = 0.5\,\text{mm}$). This should be caused by the different damping properties.

It should be noted that chatter frequencies corresponding to higher bending modes of the micro-end mills are not observed in these milling tests. If they could be detected, the identification of the operational deflection shape would be very challenging. In this case, points on the tool tip must be measured since higher modes mainly result from the deflection of the tip section.

5.2 Chatter stability in the inertial frame

The influences of the mode interaction and joint flexibility on the chatter stability are studied by the clamping conditions at the joints. At first, the first two dominant natural frequencies of several variations with respect to the translational and rotational stiffness at the tool holder–tool interface (k_t^{ht} and k_r^{ht}) as well as at the spindle–tool holder interface (k_t^{sh} and k_r^{sh}) in y-direction are compared with each other. The results are summarized in Table 3.

The first variation (corresponding to the decrease of k_t^{ht} and k_t^{sh} by 20%) and the second variation (corresponding to the decrease of only k_t^{ht} by 20%) exhibit the similar frequency values which are lower than the reference ones. It is evident that the stiffness at the tool holder–tool interface is significant for prediction of the system dynamics. As shown in the third variation, increasing k_t^{ht} by 20 % yields higher frequencies. Thus, the variations of the clamping force or torque at the tool holder–tool joint affect the system dynamics to a large extent.

From the last two variations, it can be seen that the natural frequencies are almost constant even if the rotational stiffness k_r^{ht} is decreased or increased by a factor of 10. This indicates that the rotational stiffness in the FE model is less prominent than the translational stiffness. Therefore, the assumption of the same values for both, as suggested before, is reasonable respecting the model accuracy and the simplified procedure for parameter identification.

The experimental verification is performed by varying the clamping torque M_c at the tool holder. Cutting tests are conducted using a micro-end mill with $d_t = 1\,\text{mm}$ on a brass (CuZn39Pb1) block workpiece.

Table 3 Influences of the interface stiffness on the first two dominant natural frequencies in y-direction at the nonrotating state

Stiffness variation	Mode 1 (kHz)	Mode 2 (kHz)
$k_t^{ht}, k_r^{ht}, k_t^{sh}, k_r^{sh}$ (reference)	7.203	20.970
$0.8k_t^{ht}, 0.8k_t^{sh}$ (variation 1)	6.570	20.693
$0.8k_t^{ht}$ (variation 2)	6.589	20.694
$1.2k_t^{ht}$ (variation 3)	7.712	21.260
$0.1k_r^{ht}$ (variation 4)	7.202	20.964
$10k_r^{ht}$ (variation 5)	7.204	20.971

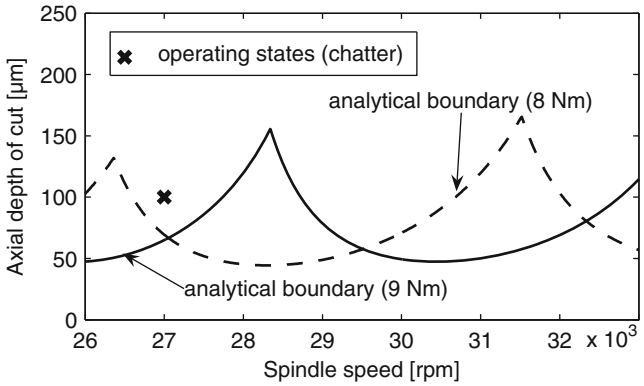

Fig. 8 Stability lobes at different clamping torques M_c

Stability behavior is studied by evaluating the response signal (the velocity of the tool shank) that is acquired using a laser vibrometer. For two clamping torques (9 and 8 Nm), chatter frequencies (5.878 and 5.281 kHz, respectively) can be detected at $n_s = 27,000$ rpm and $a_p = 100\,\mu$m. For comparison the predicted stability boundaries are computed without gyroscopic effect. As shown in Fig. 8, the results are in agreement for the two cases. Due to smaller clamping torques, the stiffness values at the tool holder–tool interface become lower. Hence, the dominant natural frequencies of the spindle system become lower, which consequently affects the chatter frequencies and the stability boundaries.

6 Conclusions

Finite element models of the spindle system and micro-end mill are presented. The gyroscopic and mode interaction effects on the dynamics and chatter stability are studied by the transfer functions and mode shapes of the FE models. Experimental validations are given by the stable as well as unstable cutting tests and the operational vibration modes. Using piezoelectric elements as in-process excitation, the transfer function of the micro-end mill in the operating state can be identified, e.g., in the form of velocity/voltage.

The gyroscopic effect on the dominant mode of the spindle system is studied in both inertial and rotating frames. In the inertial frame, the velocity-dependent skew-symmetric terms are primarily caused by the rotary inertia of the micro-end mill. Due to its much smaller mass and radius compared to the tools in conventional high-speed machining, the mode-splitting phenomenon resulting from the rotation is less significant. Thus, the gyroscopic effect on the micro-end mill dynamics and the chatter stability can be neglected. In the rotating frame, by contrast, neglecting the gyroscopic terms leads to inaccurate prediction of the tool tip dynamics.

The most flexible part in micro-milling is the micro-end mill as long as nonthin-walled workpieces are machined. Depending on the clamping condition at the interfaces of the spindle system, modeling of micro-end mills under ideal cantilever conditions is not appropriate for prediction of the tool tip dynamics. The dominant modes are strongly affected by the joint properties, especially, the tool–tool holder interface. This mode interaction effect is clearly revealed by the mode shapes of the FE models and the operational deflection shapes measured by the scanning laser vibrometer. It significantly influences the micro-end mill dynamics and the chatter stability.

Acknowledgement The authors gratefully acknowledge the financial support from the German Research Foundation (Deutsche Forschungsgemeinschaft).

References

1. Chae J, Park SS, Freiheit T (2006) Investigation of micro-cutting operations. Int J Mach Tools Manuf 46(3–4):313–332
2. Miao JC, Chen GL, Lai XM, Li HT, Li CF (2007) Review of dynamic issues in micro-end-milling. Int J Adv Manuf Technol 31:897–904
3. Novakov T, Jackson MJ (2010) Chatter problems in micro- and macrocutting operations, existing models, and influential parameters—a review. Int J Adv Manuf Technol 47:597–620
4. Vogler MP, Kapoor SG, DeVor RE (2004) On the modeling and analysis of machining performance in micro-endmilling, part II: cutting force prediction. ASME J Manuf Sci Eng 126(4):695–705
5. Liu X, DeVor RE, Kapoor SG (2006) An analytical model for the prediction of minimum chip thickness in micromachining. ASME J Manuf Sci Eng 128(2):474–481
6. Jun MBG, Liu X, DeVor RE, Kapoor SG (2006) Investigation of the dynamics of microend milling—part I: model development. ASME J Manuf Sci Eng 128(4):893–900
7. Chatterjee S (1996) Spindle deflections in high-speed machine tools—modelling and simulation. Int J Adv Manuf Technol 11:232–239
8. Chen JS, Hwang YW (2006) Centrifugal force induced dynamics of a motorized high-speed spindle. Int J Adv Manuf Technol 30:10–19
9. Movahhedy MR, Mosaddegh P (2006) Prediction of chatter in high speed milling including gyroscopic effects. Int J Mach Tools Manuf 46(9):996–1001
10. Rivin EI (2000) Tooling structure: interface between cutting edge and machine tool. CIRP Ann - Manuf Technol 49(2):591–634
11. Mascardelli BA, Park SS, Freiheit T (2008) Substructure coupling of microend mills to aid in the suppression of chatter. ASME J Manuf Sci Eng 130(1):011010

12. Shi Y, Mahr F, von Wagner U, Uhlmann E (2011) Mode-dependent chatter stability in micro milling: structural modeling and experiments. In: Proc 4th international conference on mechanical engineering and mechanics, Suzhou, China
13. Marui E, Ema S, Kato S (1987) Contact rigidity at tool shank of turning tools. ASME J Eng Ind 109(2):169–172
14. Smith S, Jacobs TP, Halley J (1999) The effect of drawbar force on metal removal rate in milling. CIRP Ann - Manuf Technol 48(1):293–296
15. Luo X, Cheng K, Ward R (2005) The effects of machining process variables and tooling characterisation on the surface generation. Int J Adv Manuf Technol 25:1089–1097
16. Albertelli P, Cau N, Bianchi G (2011) The effects of dynamic interaction between machine tool subsystems on cutting process stability. Int J Adv Manuf Technol. doi:10.1007/s00170-011-3465-5
17. Schmitz TL, Donaldson RR (2000) Predicting highspeed machining dynamics by substructure analysis. CIRP Ann - Manuf Technol 49(1):303–308
18. Park SS, Altintas Y, Movahhedy M (2003) Receptance coupling for end mills. Int J Mach Tools Manuf 43(9):889–896
19. Park SS, Chae J (2008) Joint identification of modular tools using a novel receptance coupling method. Int J Adv Manuf Technol 35:1251–1262
20. Duncan GS, Tummond M, Schmitz TL (2005) An investigation of the dynamic absorber effect in high-speed machining. Int J Mach Tools Manuf 45(4–5):497–507
21. Zatarain M, Bediaga I, Muñoa, J, Insperger T (2010) Analysis of directional factors in milling: importance of multi-frequency calculation and of the inclusion of the effect of the helix angle. Int J Adv Manuf Technol 47:535–542
22. Filiz S, Ozdoganlar OB (2008) Microendmill dynamics including the actual fluted geometry and setup errors—part II: model validation and application. ASME J Manuf Sci Eng 130(3):031120
23. Filiz S, Ozdoganlar OB (2011) A three-dimensional model for the dynamics of micro-endmills including bending, torsional and axial vibrations. Precis Eng 35(1):24–37
24. Hagedorn P, von Wagner U (2004) "Smart pads": a new tool for the suppression of brake squeal? VDI-Berichte 575 (ed. B. Breuer). In: Proc XXIV. μ-Sympsoium:153–172, Bad Neuenahr
25. von Wagner U, Hochlenert D, Jearsiripongkul T, Hagedorn P (2004) Active control of brake squeal via "smart pads". SAE Int J Passeng Cars - Mech Syst 113(6):1186–1192
26. von Wagner U, Schlagner S (2007) Beurteilung des Geräuschverhaltens von Scheibenbremsen mit Hilfe von piezokeramischen Aktoren und Sensoren (in German). VDI-Berichte 1982:151–165
27. von Wagner U, Schlagner S (2009) On the origin of disk brake squeal. Int J Veh Des 51(1–2):223–237
28. Nelson HD (1980) A finite rotating shaft element using Timoshenko beam theory. J Mech Des 102(4):793–803
29. Ewins DJ (1986) Modal testing: theory and practice. Brüel & Kjær
30. Schauer K (2006) Entwicklung von Hartmetallwerkzeugen für die Mikrozerspanung mit definierter Schneide (in German). Dissertation, Technische Universität Berlin
31. Kivanc EB, Budak E (2004) Structural modeling of end mills for form error and stability analysis. Int J Mach Tools Manuf 44(11):1151–1161
32. Namazi M, Altintas Y, Abe T, Rajapakse N (2007) Modeling and identification of tool holder-spindle interface dynamics. Int J Mach Tools Manuf 47(9):1333–1341
33. Altintas Y (2000) Manufacturing automation. Cambridge University Press, UK
34. Altintas Y, Budak E (1995) Analytical prediction of stability lobes in milling. CIRP Ann - Manuf Technol 44(1):357–362
35. Park SS, Qin YM (2007) Robust regenerative chatter stability in machine tools. Int J Adv Manuf Technol 33:389–402